AIAA Propulsion and Energy Forum
August 24-28, 2020, VIRTUAL EVENT
AIAA Propulsion and Energy 2020 Forum

10.2514/6.2020-3617

Performance of a 9-kW Magnetically-Shielded Hall Thruster with Krypton

AIAA-2020-3617

Presented at the AIAA Propulsion and Energy Forum
August 24–26, 2020

Leanne L. Su,* Alexander R. Vazsonyi,† and Benjamin A. Jorns‡
University of Michigan, Ann Arbor, MI, 48109

The performance of a 9-kW magnetically-shielded Hall thruster operating on xenon and krypton is characterized. The anode efficiencies were measured with a thrust stand at several conditions from 300 V to 600 V and 15 A to 20 A, and a probe suite was used to estimate the specific efficiency modes at the 300 V, 4.5 kW condition. It was found that the difference between krypton and xenon efficiency increased from the typical, historical value of approximately 5-15% on unshielded thrusters to a gap of 9-19% on the shielded thruster. This increase is primarily attributable to the differences in mass utilization and current utilization efficiencies between krypton and xenon, possibly caused by lower electron temperatures at the wall and higher electron mobility. The results of the study are discussed in the context how the operation of krypton on a magnetically-shielded Hall thruster may be fundamentally different from operation on xenon and potential pathways into the improvement of performance on krypton.

Nomenclature

D_T	thruster diameter (channel centerline)
I_b	ion beam current
I_d	discharge current
P_d	discharge power
R	radial distance
T	thrust
T_e	electron temperature
V_a	acceleration voltage
V_d	discharge voltage
V_p	plasma potential
V_{MPCL}	most probable voltage along centerline
Z_i	charge state of the i^{th} ion species
Ω_i	current fraction of the i^{th} ion species
$\dot{m}_a$	anode mass flow rate
$\dot{m}_b$	ion beam mass flow rate
η_a	anode efficiency
η_b	current utilization efficiency
η_d	plume divergence efficiency
η_m	mass utilization efficiency
η_q	charge utilization efficiency
η_v	voltage utilization efficiency
λ_{MFP}	mean free path
σ_{iz}	ionization cross-section
θ_d	plume divergence angle
ε	energy
ξ	exchange ratio, $\frac{m_n I_d}{\dot{m}_a e}$
g_0	gravitational acceleration
j	current density

*Ph.D. Candidate, Department of Aerospace Engineering, AIAA Student Member, leannesu@umich.edu
†Ph.D. Candidate, Department of Aerospace Engineering, AIAA Student Member, vazsonyi@umich.edu
‡Assistant Professor, Department of Aerospace Engineering, AIAA Senior Member, bjorns@umich.edu.

k_{iz}	ionization rate
m_e	electron mass
m_n	neutral mass
n_e	electron density
n_n	neutral density
r	radial position
v_r	radial velocity
v_y	axial velocity
w_{iz}	ionization region width

I. Introduction

Hall effect thrusters (HETs) are electric propulsion devices that have been used on satellites for station-keeping and orbit-raising for decades. While traditionally Hall thrusters have used xenon as propellant, krypton has also been proposed as a potentially attractive alternative propellant to xenon. Krypton can achieve a higher specific impulse at the same discharge voltages and is up to ten times cheaper [1]. These features have the potential to enable an expanded mission space for Hall thrusters. However, the use of krypton HETs has traditionally been avoided due to poor mass utilization efficiency [2, 3]. The anode efficiencies of thrusters operated with krypton historically have been measured at 5-15% lower than efficiencies for thrusters operated with xenon [2–9], although smaller efficiency gaps have been measured on a Hall thruster designed for krypton operation [10, 11]. This performance gap has largely precluded the use of krypton-based Hall thrusters in flight, with the recent and notable exception of the Starlink system from SpaceX.

With that said, the studies contrasting xenon to krypton performance to date have been limited to thrusters with traditional magnetic field configurations. The recent advent of magnetic shielding technology may ultimately change these trends. Magnetic shielding is a technique developed to extend Hall thruster lifetimes by shaping the magnetic field lines such that energetic ions do not impact channel walls [12, 13]. While this change in magnetic field configuration has been shown to drastically increase lifetime, it has been noted that this shielding also impacts a number of other physical phenomena in the thrusters. For example, compared to unshielded (US) thrusters, magnetically-shielded (MS) thrusters operate at higher electron temperatures and have acceleration regions located further downstream [12, 14].

These changes in the plasma state may combine in a way such that the factors influencing the performance gap between xenon and krypton are fundamentally different than they are in an unshielded thruster. For instance, the higher electron temperatures in the channel of a shielded thruster lead to higher ionization cross-sections, a phenomenon that could benefit krypton more than xenon because krypton cross-sections increase more for a given increase in electron temperature compared to xenon [15]. This could reduce the known efficiency gap in mass utilization between xenon and krypton. On the other hand, the shift of the acceleration region downstream in shielded thrusters may also disproportionately impact the divergence efficiency of the less massive and more mobile krypton. This may cause the efficiency gap between krypton and xenon to worsen for shielded thrusters.

Given the many advantages of krypton and the increasing adoption of shielded thrusters, there is an apparent need for a systematic investigation into the changes in performance for xenon versus krypton on a shielded thruster. To this end, the goal of this work is to compare the performance—thrust, specific impulse, and efficiency—of a 9-kW class magnetically-shielded Hall thruster operating on krypton and xenon. We begin by reviewing a theoretical framework for the various contributions to Hall thruster efficiency. We then present the experimental setup we employed for characterizing these different contributions. Next, we present the results of our study, including trends in anode efficiency as well as a breakdown of contributions towards efficiency losses. Finally, we include a discussion of why the differences in performance may exist. These results are discussed in the context of future efforts to develop a magnetically-shielded Hall thruster optimized for krypton operation.

II. Efficiency Model for Hall Thrusters

In this section we present an overview of the key metrics for evaluating thruster performance. This provides a common framework for contrasting the operation of xenon and krypton. The thrust, T, and specific impulse, I_{sp}, of the thruster are related through the following expression: $I_{sp} = T/(\dot{m}g_0)$, where $\dot{m}$ is the total mass flow rate and g_0 is the gravitational acceleration. The anode efficiency is a measure of the ratio of the kinetic power in the exhaust to the discharge power in the device, $\eta_a = T^2/(2\dot{m}_a P_d)$, where $\dot{m}_a$ is the anode mass flow and P_d is the discharge power. This latter parameter is calculated from $P_d = V_d I_d$, where V_d is the applied discharge voltage of the circuit and I_d is the measured discharge current. The anode efficiency neglects losses from the cathode flow and electromagnets, thus allowing us to more directly evaluate the efficiency of a thruster isolated from the larger system.

In this work, we directly measure the anode efficiency from performance measurements; we further try to explain the trends in these measured efficiencies by considering the various contributions to this parameter. This breakdown is based on the the Hall thruster efficiency model developed by Hofer [16–19], which defines the anode efficiency as the product of the five contributions:

$$\eta_a = \eta_b \eta_v \eta_d \eta_q \eta_m. \tag{1}$$

where η_b is the current utilization efficiency, η_v voltage utilization efficiency, η_d is the plume divergence efficiency, η_q is charge utilization efficiency, and η_m is the mass utilization efficiency. Each of these contributions can be inferred from measurements of the plume properties of the plasma. In particular, we have the following prescriptions:

- *Current utilization efficiency*: The fraction of ion current contained in the discharge current is defined as

$$\eta_b = \frac{I_b}{I_d}, \tag{2}$$

  where I_d is the discharge current and I_b is the ion beam current.

- *Voltage utilization efficiency*: The conversion of voltage into ion velocity is defined as

$$\eta_v = \frac{V_a}{V_d}, \tag{3}$$

  where V_d is the discharge voltage and V_a is the average acceleration voltage.

- *Plume divergence efficiency*: The decrease in axially-directed momentum from divergence of the ion beams is defined as

$$\eta_d = (\cos\theta_d)^2, \tag{4}$$

  where θ_d is the angle of plume divergence from channel centerline.

- *Charge utilization efficiency*: The decrease in efficiency from multiply-charged ions in the beam is defined as

$$\eta_q = \frac{\left(\sum \frac{\Omega_i}{\sqrt{Z_i}}\right)^2}{\sum \frac{\Omega_i}{Z_i}}, \tag{5}$$

  where Ω_i is the current fraction of the i^{th} charge ion species, $\frac{I_i}{I_d}$, and Z_i is the charge state of the i^{th} ion species.

- *Mass utilization efficiency*: The conversion of neutral mass flux into ion mass flux is defined as

$$\eta_m = \frac{\dot{m}_b}{\dot{m}_a} = \frac{\frac{m_i I_b}{e} \sum_i \frac{\Omega_i}{Z_i}}{\dot{m}_a} = \xi \eta_b \sum \frac{\Omega_i}{Z_i}, \tag{6}$$

  where $\dot{m}_a$ is anode mass flow rate, $\dot{m}_b$ is the ion beam mass flow rate, m_i is the ion mass, and ξ is a value defined as the exchange ratio.

We can use this model for the breakdown of the anode efficiency to identify what specific processes within the thruster are primarily contributing to any losses. By measuring each of these efficiency components, we can also compare the anode efficiency calculated by taking the product of all five efficiency modes $\eta_{a,probe}$ to the anode efficiency calculated with the thrust, anode mass flow rate, and discharge power, $\eta_{a,thrust}$.

III. Experimental Setup

In this section, We outline the conditions at which we operated the thruster for both xenon and krypton. We describe the thruster, test facility, and diagnostics used for the experiment, as well as our approach to uncertainty quantification.

A. Thruster and Test Facility

We conducted an experimental study to compare the different efficiency modes of a magnetically-shielded Hall thruster on xenon and krypton. We used the H9, a 9-kW magnetically-shielded Hall thruster developed in partnership between the University of Michigan (UM), Jet Propulsion Laboratory (JPL), and the Air Force Research Laboratory (AFRL). Copies of this thruster, shown in Fig. 1a, exist at UM, JPL, AFRL, and the Georgia Institute of Technology [20]. We used a centrally-mounted LaB6 cathode [21] operating at a fixed 7% cathode flow fraction. The thruster ran in cathode-tied mode at all conditions.

All tests were conducted at the University of Michigan in the Large Vacuum Test Facility (LVTF), a chamber 6 m in diameter and 9 m in length capable of pumping ~500 kL/s of xenon and ~600 kL/s of krypton [22], shown in Fig.1b. Pressures in the chamber were measured with Stabil ion gauge calibrated for xenon, mounted 1 m away from the thruster in the thruster exit plane and pointing downstream as shown in Fig. 3 following industry standards [23]. Background pressure at each operating condition are shown in Table 1, with pressure readings converted for each gas.

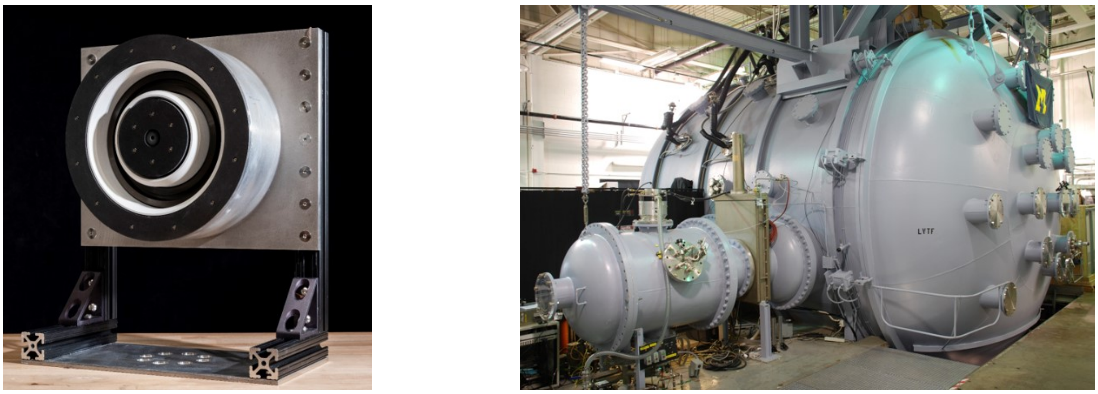

(a) (b)

Fig. 1 a) The H9, a 9-kW magnetically-shielded Hall thruster and b) the Large Vacuum Test Facility at the University of Michigan.

The operation of xenon and krypton on the H9 was compared at the same power across multiple operating conditions that are summarized in Table 1. We adjusted flow rates to achieve the nominal current levels for both xenon and krypton. At each condition, we optimized the magnetic field strength for the lowest discharge current oscillations. Flow rates and magnet settings were adjusted via a data acquisition system (DAQ). During each day of testing, we allowed the thruster to run for at least two hours or until reaching thermal steady-state (defined as no more than 1° C change in temperature per minute) before taking any measurements with the thrust stand or probe suite. When increasing the current or voltage, the thruster ran at the higher power level for at least ten minutes before we took probe measurements.

Voltage (V)	Current (A)	Power (kW)	Xe Pressure (μtorr)	Kr Pressure (μtorr)
300	15	4.5	4.58	4.66
300	20	6	5.60	5.93
400	15	6	4.82	4.60
500	15	7.5	5.00	4.99
600	15	9	5.18	5.18

Table 1 Nominal operating conditions and background pressures for xenon and krypton.

B. Diagnostics

We used a null-type inverted pendulum thrust stand to collect thrust data at all conditions. The thrust stand used double-ended pivot bearings and a series of weights for calibration [24, 25]. The thrust stand has an uncertainty of

±3 − 5 mN. For each thrust point, we leveled and recorded the current to the thrust stand while the thruster was running, then shut off the gas and power to the thruster simultaneously. After thruster shutoff, we leveled and read the current again. This difference in current was then used with a calibration curve from the weights to determine thrust at each point. We used the thrust and operational data from the DAQ to calculate the anode efficiency. The DAQ also measured temperature through thermocouples mounted at the thruster face, body, back plate, and anode to monitor thruster health.

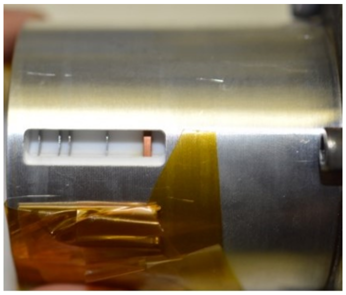

(a)

(b)

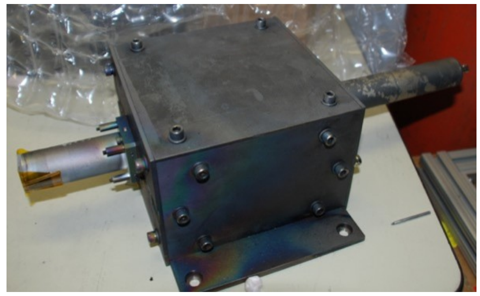

(c) .

Fig. 2 a) Side view of the RPA, b) unmounted Faraday probe, and c) E×B probe used in the probe suite.

To evaluate the different contributions to efficiency (Eq. 1), we used a probe suite consisting of a retarding potential analyzer (RPA), Langmuir probe (LP), far-field Faraday probe (FFFP), and E×B probe to interrogate the discharge plasma. The RPA consists of a series of grids that selectively filters ions based on energy level. The sweeper grid is set from 0 to twice the operating voltage of the thruster, and the slope of the resultant current trace indicates the most likely energy level of the ions, correlating to a most probable accelerating voltage. The RPA has a 6.45 cm^2 aperture with four grids and a collector inside. We set both the primary and secondary electron suppression grids to -30 V and swept the ion selection grid from 0 to ∼ 2× the discharge voltage.

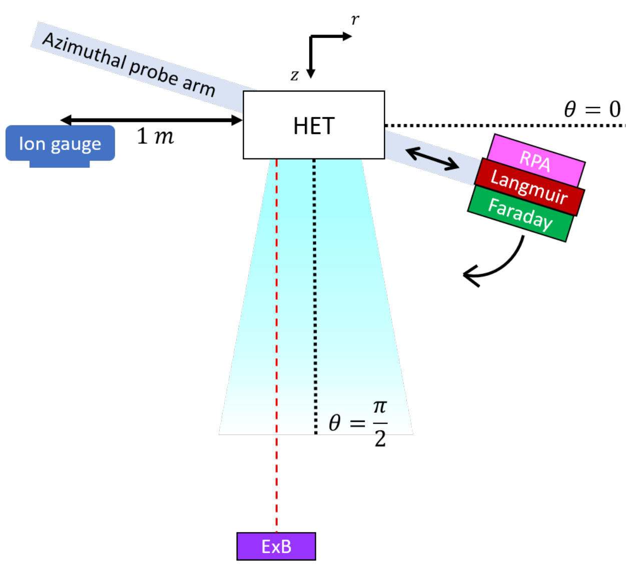

Fig. 3 Diagram of probe and thruster setup within the chamber.

Langmuir probes are commonly used to evaluate various properties of a plasma by inserting an electrode into the plasma, applying voltage to it, and measuring the current collected. The resultant I-V curve yields information about the plasma potential, electron temperature, and more. The Langmuir probe we used consists of a 1 mm thoriated tungsten filament routed through a ceramic tube, biased from ∼-5 to ∼15 V.

A Faraday probe acts similarly to a Langmuir probe, with a metal plate biased to voltage such that it measures only the ion saturation current. A guard ring around the central probe is used to maintain a constant effective probe area. By taking a Faraday probe trace at multiple azimuthal locations, we can plot a distribution of the current density throughout the plume of the thruster and determine both the beam current and divergence angle. The FFFP used has a 1.74 cm inner diameter molybdenum collector and 2.38 cm outer diameter molybdenum guard ring, with a 0.05 gap between them. It is isolated with a ceramic spacer mount.

An E×B probe measures ion velocity, a proxy for charge state, by utilizing an internal electric field set orthogonal to an internal magnetic field. When the fields are balanced for an ion entering at a given speed as determined by its charge, the ion will be able to pass through the probe without colliding into a wall and be collected at the exit. The electric field in the probe is varied by adjusting the voltage to a set of electrical plates. We used an E×B probe with an entrance aperture 1.6 mm in diameter, an entrance collimator 7.5 cm long, an exit collimator 15 cm long, and electrical plates spaced 0.97 cm apart. The peak magnetic field is 0.16 T in the center of the probe. We swept the applied bias voltage to the plates from 0 to 70 V. The RPA, Faraday probe, and E×B probe are shown in Fig. 2.

We mounted the RPA, LP, and FFFP on a radial probe arm with movement in the radial and azimuthal directions. We took measurements for the RPA and LP at 90° from approximately 6, 8, and 10 thruster diameters D_T downstream. The FFFP was swept from 0° to 80° in increments of 5°, then to 100° in increments of 1° before returning to 0° in the same increments. These sweeps were performed at the same three downstream locations. The E×B probe was mounted in a fixed position approximately 10 D_T downstream, aligned to the center of the thruster channel at the 9 o'clock position. Figure 3 shows the notional probe setup within the chamber with r pointing in the radial direction and z pointing in the axial direction.

IV. Data Analysis Methods

In order to evaluate the voltage utilization efficiency in Eq. 3, it is necessary to determine the acceleration energy of the beam. To this end, we employed a combination of the RPA and Langmuir probe. These probes measure the most probable accelerating voltage along centerline and the plasma potential, respectively:

$$V_a = V_{MPCL} + V_p. \tag{7}$$

The RPA energies are biased with respect to ground, which is why we need to account for the correction of the plasma potential with the Langmuir probe. Figure 4 shows the raw current trace and derivative of current collected by the RPA, with the most probable voltage determined by the maximum of the derivative. The plasma potential is the point of the I-V curve measured by the Langmuir probe where the second derivative goes to zero [26]. An example trace is shown in Fig. 5.

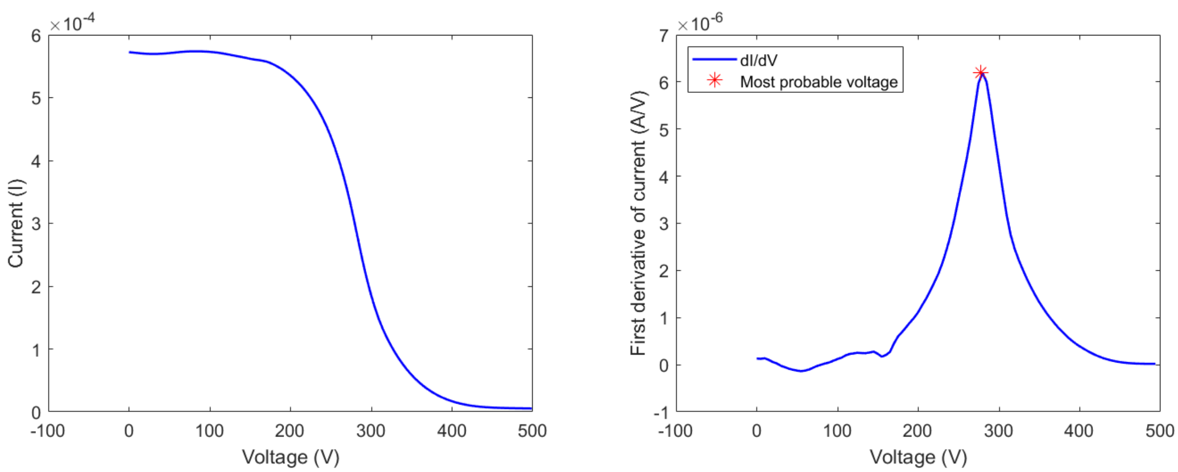

(a) (b)

Fig. 4 Plots of the a) raw current and b) derivative of current collected by the RPA at 90 degrees for xenon at 300 V, 15 A.

We used a bootstrapping method to determine 95% confidence intervals on the estimates for acceleration potential [27]. In particular, the raw trace for each probe was resampled randomly, and each resample was fitted with a spline; the most probable voltage along centerline and plasma potential were then determined by the derivatives of these fitted curves for the RPA and LP, respectively. This method was run through a thousand iterations.

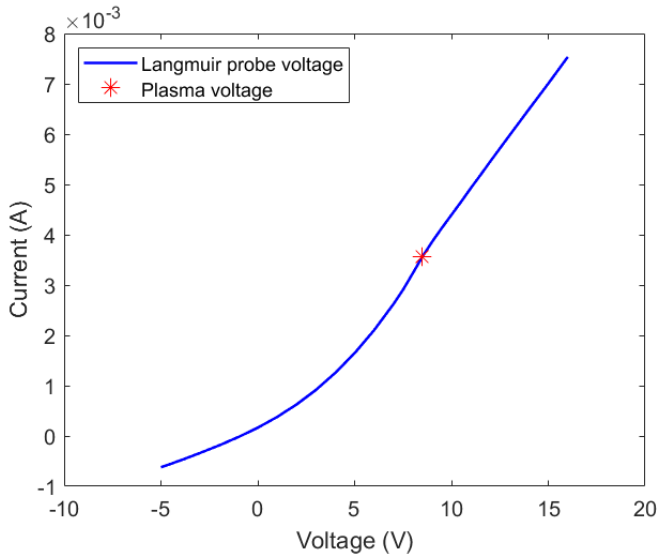

Fig. 5 Raw current collected by the Langmuir probe at 90 degrees for xenon at 300 V, 15 A.

In order to estimate the beam current utilization efficiency, Eq. 2, we used the far field Faraday measurements of ion current density. Since the probe arm was swept from 0° to 100°, we averaged each measurement based on its distance from centerline at 90°. The resultant data was then mirrored about centerline for a full trace, shown in Fig. 6.

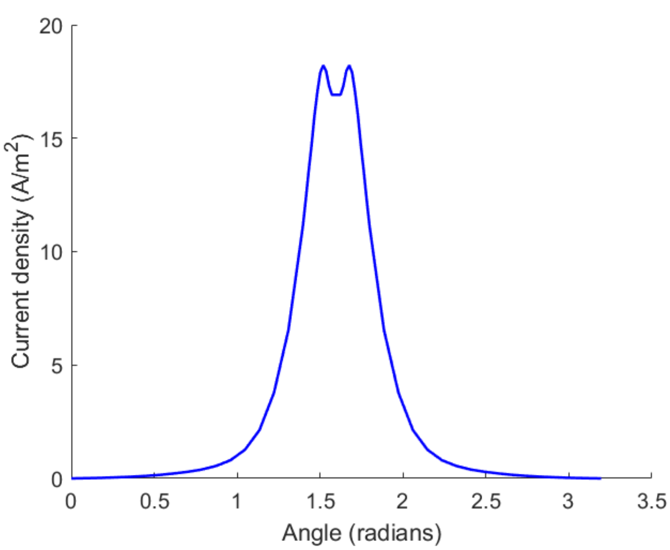

Fig. 6 Processed data collected by the far-field Faraday probe for xenon at 300 V, 15 A from 10 D_T downstream as a function of angle measured with respect to the thruster plane.

The beam current was calculated through an integration of both the raw far-field Faraday probe trace and a flat subtraction of the current measured at 30° to account for charge exchange ions (CEX) with Eq. 8. In this equation, R is the downstream distance from thruster centerline to the Faraday probe, and j is the current density equivalent to the collected current divided by probe area, I_{probe}/A_{probe}. The CEX-subtraction method has been used before in the absence of a controlled-background pressure study [28, 29]. The 30° value was determined by an azimuthal sweep with the RPA at a 300 V, 10 A condition that showed a prominent CEX population beginning at 30° and extending to larger angles. These values were averaged over traces taken at D_T = 6, 8, and 10.

$$I_b = 2\pi R^2 \int_0^{\pi/2} j(\theta) \cos\theta d\theta \tag{8}$$

In order to estimate the divergence efficiency, Eq. 4, we used the FFFP measurements of ion current density. We calculated the divergence angle with the following equation, using the aforementioned CEX-subtraction and raw traces for the current trace [28, 30]:

$$\cos\theta_d = \frac{\int_0^{\pi/2} j(\theta) \cos\theta \sin\theta d\theta}{\int_0^{\pi/2} j(\theta) \cos\theta d\theta} \tag{9}$$

For the beam current and divergence angle, we treated the values calculated from the raw and CEX-subtraction traces as the sample dataset. A thousand-iteration bootstrapping method was then used to determine the 95% confidence intervals on these values.

In order to estimate the charge utilization efficiency, we used the E×B probe, which was aligned to channel centerline at the 9 o'clock position. Figure 7 shows an example of a raw trace from this data. We used a series of four two-peak Gaussian fits to determine the ratio of each current species Ω_i from the current collected by the E×B probe. This fit has previously been shown to accurately capture the distribution of each species [28], and the two-peak Gaussian specifically proved to be the best fit during the analysis process as determined by residuals, shown as the thick blue line in Fig. 7.

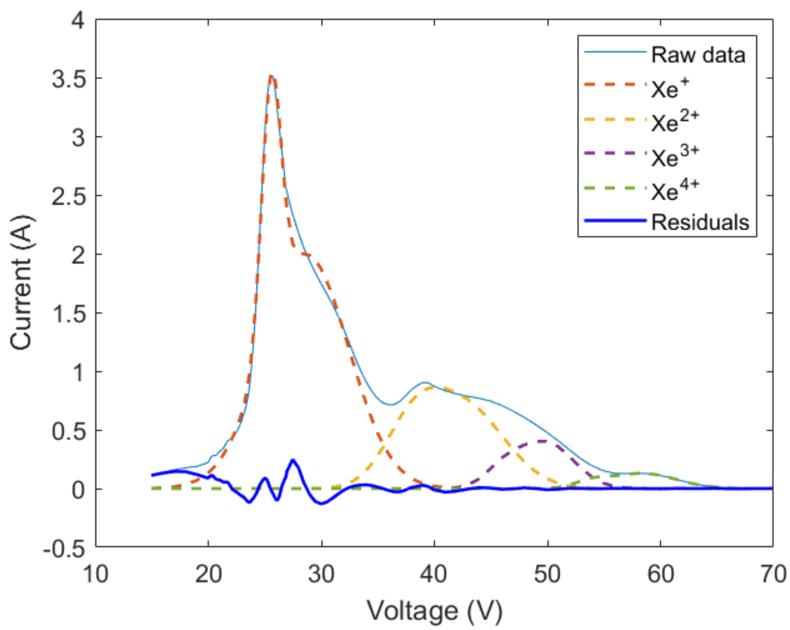

Fig. 7 Current collected by E×B probe for xenon at 300 V, 15 A, with two-peak Gaussian fits for each species.

For the uncertainty in the E×B probe measurements, we used a 95% confidence interval from a distribution of the residuals under each peak to determine the uncertainty in each Ω_i individually. The residuals here were determined by subtracting the fitted two-peak Gaussians from the raw curve and taking the absolute value of the result.

V. Results

Armed with the theoretical description and experimental setup from the previous sections, we present here our results of thrust, specific impulse, and anode efficiencies at all conditions, as well as a breakdown of anode efficiency at the 300 V, 15 A condition for xenon and krypton.

A. Trends in Overall Performance

Figure 8 shows the specific impulse and thrust measured at each condition for xenon and krypton on the H9. The specific impulse of xenon increases linearly for the 300 V conditions with power, while the krypton specific impulse increases approximately linearly up to 500 V, 15 A, then increases by much less to the 600 V, 15 A condition. This dip results in the specific impulse of krypton actually being lower than that of xenon at the 9-kW condition, with the specific impulse at all conditions calculated with the total mass flow through the thruster.

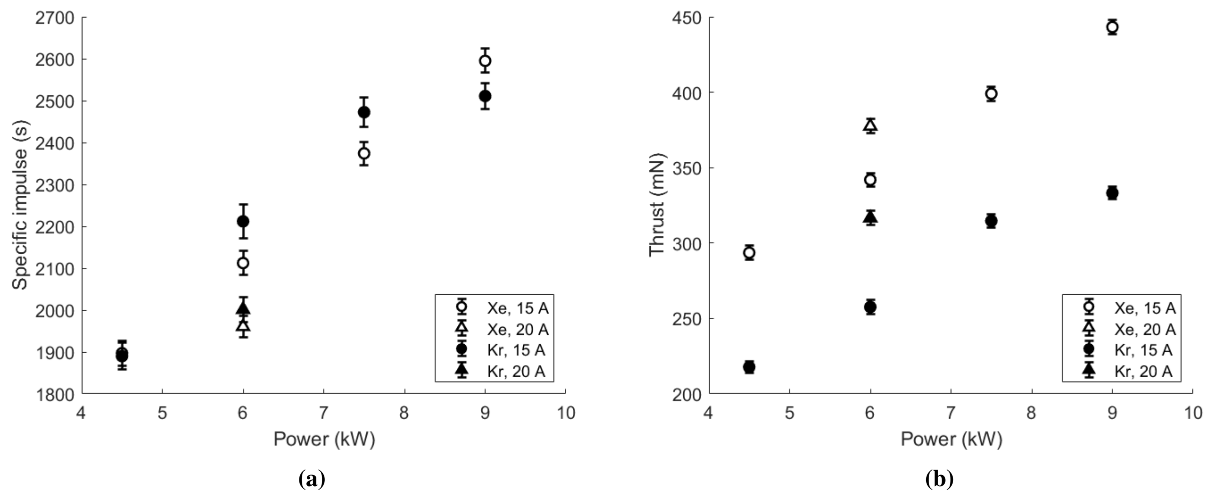

Fig. 8 Comparison of a) specific impulse and b) thrust for xenon and krypton at different conditions.

The anode efficiencies are shown Fig. 9. The efficiencies measured for xenon match previous measurements on the H9 to within uncertainty [31]. As reflected by the trends in specific impulse and thrust, the anode efficiency of krypton drops significantly from 500 V to 600 V. At each condition, the efficiency of krypton is 9-19% lower than that of xenon.

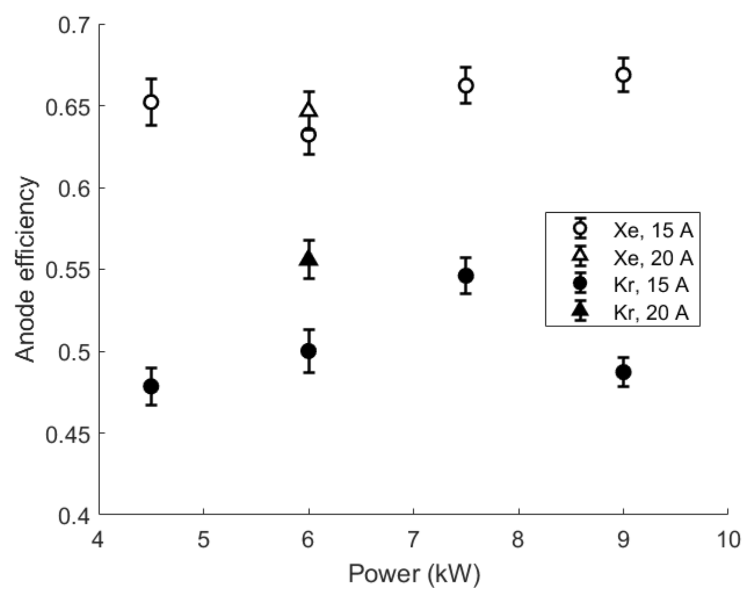

Fig. 9 Comparison of anode efficiencies for xenon and krypton at different conditions.

B. Comparison of Efficiencies

While the anode efficiency results unambiguously show that the performance of the H9 on krypton is lower than with xenon, it is not immediately evident why this is this case. To further elucidate this, we now consider the probe-based measurements of the different contributions to efficiency. We note that we only have a dataset for one operating condition for this comparison at 300 V and 15 A.

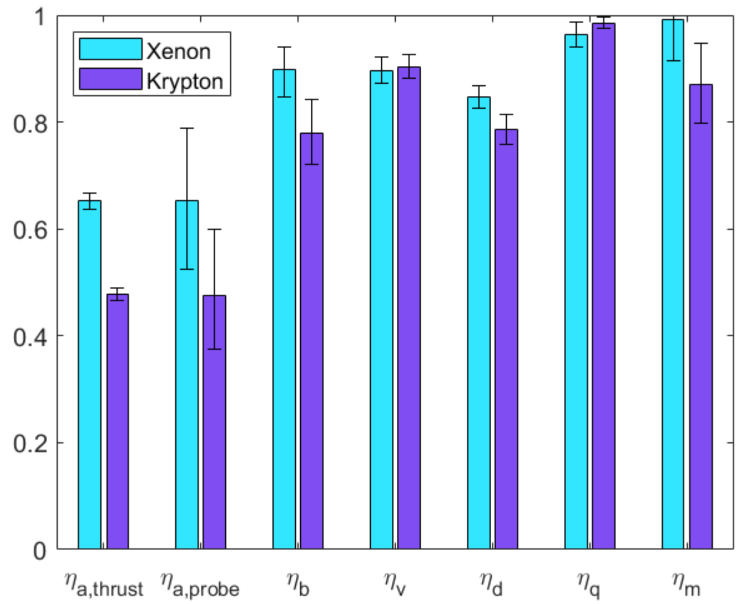

Fig. 10 Comparison of anode efficiencies, measured by the thrust stand $\eta_{a,thrust}$ and probe suite $\eta_{a,probe}$, as well as specific efficiency contributions (from left to right: current, voltage, divergence, charge, and mass) for xenon and krypton at 300 V, 15 A.

Figure 10 shows a plot of the the anode and efficiencies. These values are also listed in Table 2. For measurements where the uncertainty was not equal in the positive and negative directions, we took an average for Table 2. The probe-measured anode efficiencies match the thrust stand-measured anode efficiencies to within uncertainty, although the probe-measured uncertainties are relatively large at approximately ±12%. This is primarily the result of the uncertainty in the beam current utilization efficiency, which propagates through the mass utilization efficiency and again to the anode efficiency. Despite these margins, the trends in the efficiencies between xenon and krypton are still apparent. The largest disparities in efficiency between xenon and krypton are found in the mass utilization and beam utilization efficiencies, with a smaller disparity between the divergence efficiencies. These differences between xenon and krypton are approximately 12% for η_b, 12% for η_m, and 6% for η_d. The major contributors to the difference in anode efficiencies are therefore the current utilization, mass utilization, and divergence efficiencies. We turn in the next section to contextualizing this result with respect to previous reports of unshielded krypton thrusters.

VI. Discussion

While the results in the previous section show that the performance of krypton on the H9 is lower than that of xenon, we remark here that these results are not identical to previous xenon/krypton comparisons that have been performed on Hall thrusters with a more traditional magnetic field configuration. First, as shown in Fig. 9, the performance gap does not close with higher voltage. Second, the change in performance is different in magnitude than those previously reported for unshielded thrusters. The overall gap in anode efficiency at a given condition between xenon and krypton has increased from 5-15% to 9-19% from unshielded thrusters to the H9. In addition, previous comparisons of efficiencies on an unshielded thruster showed a 3% gap in η_b and a 11% gap in η_m between xenon and krypton [2], while we see a 12% gap in both for the H9. We discuss these results as well as their potential causes in more detail in the following section.

Efficiency	Xe Value	Xe Uncertainty	Kr value	Kr Uncertainty
$\eta_{a,thrust}$	65.2%	±1.4%	47.9%	±1.1%
$\eta_{a,probe}$	64.8%	±13%	47.7%	±11%
η_b	89.6%	±4.4%	78.1%	±5.8%
η_v	89.7%	±2.3%	90.3%	±2.4%
η_d	84.7%	±2.0%	78.8%	±2.7%
η_q	96.4%	±2.3%	98.5%	±1.1%
η_m	98.9%	±7.1%	87.2%	±7.3%

Table 2 Anode and specific efficiencies measured for xenon and krypton at 300 V, 15 A.

A. Trends with Discharge Voltage

Unlike previous measurements on an unshielded Hall thruster [2], the performance gap between krypton and xenon does not close at higher voltages and in fact widens between the 500 V and 600 V conditions. The reason for this trend is not immediately apparent. One possible correlational explanation is the anomalously high oscillations seen at high-voltage conditions for krypton operation. Indeed, thrust measurements taken at the 500 V, 15 A condition showed that thrust decreased exponentially as the discharge current oscillations increased. The cause for the changes in these oscillations is unknown at this time, but may be the cause of the decrease in performance at the high-power condition for krypton. The steady-state anode temperature of krypton was also more than 100 K higher than that of xenon and increased with power, which may have contributed to the loss in efficiency at high-voltage conditions due to thermal radiation.

B. Comparison of Efficiencies between MS and US Thrusters

Our results indicate that the current utilization efficiency gap between xenon and krypton worsened when switching from an unshielded to a shielded thruster, while the mass utilization efficiency gap stayed approximately the same. Previous measurements of the divergence efficiency for krypton on an unshielded thruster vary across different thrusters based on geometry and power [9, 32, 33] and are therefore difficult to compare to our shielded results. Additionally, we should note that various differences exist between the H9 and previous Hall thrusters that have operated with krypton beyond the presence of magnetic shielding. Many of these previous studies were conducted with Hall thrusters at different operating powers and with different design heritages [2–9], so the differences in efficiency may be partially due to reasons beyond magnetic shielding. However, our results still indicate that shielding could be one of the causes for the larger performance drop from xenon to krypton. With this in mind, we discuss in the following section possible differences caused by shielding that may explain the increase in efficiency gap between the H9 and previous reports of unshielded thrusters.

One possible cause for the lower krypton divergence efficiency is that the acceleration region moves downstream on the krypton MS thruster, causing ions to be accelerated more radially rather than axially. Previous work has shown that acceleration region is pushed downstream by switching from a US to MS thruster [12, 14] and by switching from xenon to krypton [34, 35]. Shielding and krypton operation combined may then push the acceleration region out even further to the point where it is significantly downstream of the exit plane. If this is indeed happening, we would then expect the divergence efficiency of krypton MS operation to decrease compared to xenon. The results in Fig. 10 indicate that the divergence efficiency of krypton is approximately 5% less than that of xenon, both with uncertainties of 2-3%. The range of divergence efficiency measurements for krypton on unshielded thrusters make it difficult to compare the impact of shielding directly.

For the current utilization, we remark that the gap in η_b is minimal on a US thruster at 3%, jumping to 12% for the MS thruster [2]. The culprit of this increase may be an increase in electron mobility. A lower current utilization efficiency is associated with a higher electron current, meaning that the electron current increased more from xenon to krypton on MS thrusters than on US thrusters. This may indicate that shielding increases the electron mobility for krypton operation. Unfortunately, electron mobility is still a poorly-understood phenomenon in Hall thrusters; at this time we cannot point quantitatively to which features of shielding might lead to higher mobility for krypton as compared to unshielded thrusters.

While we do not have sufficient data or physical understanding to point to the underlying causes for differences in krypton/xenon operation for US/MS thrusters, we can remark more quantitatively on the mass utilization. In particular, it is intriguing that the mass utilization appears to be approximately the same even though the magnetic field geometries are notably different. We expand upon this result in more detail in the following.

1. Exit Plane Neutral Density

The mass utilization efficiency, expressed in Eq. 6, is an indicator of how effectively the thruster is ionizing incoming neutrals. We would then expect the mean free path of ionization to be lower for higher values of mass utilization efficiency because a shorter mean free path means a higher likelihood of ionization while the neutrals are within the channel. The mean free path of ionization can be expressed as

$$\lambda_{MFP} = \frac{1}{\sigma_{iz} n_n}, \tag{10}$$

where σ_{iz} is the ionization cross-section and n_n is the neutral density. For krypton to have a lower ionization rate, reflected in its lower η_m, we would expect that the ionization cross-section and/or the neutral density of krypton is lower, causing a higher mean free path and therefore less ionization. Indeed, previous work has indicated that Hall thrusters can be optimized for krypton by extending the channel lengths and allowing more time for the neutrals to ionize [10, 11].

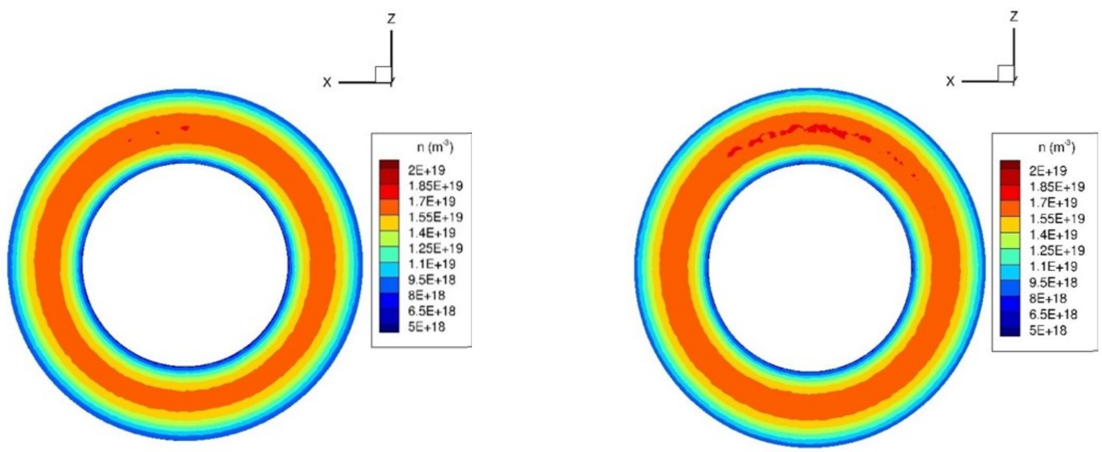

(a) **(b)**

Fig. 11 Simulations of a) xenon and b) krypton neutral densities at the exit plane of the H9.

We ran a simulation of neutral flow through the channel of the H9 using the direct-simulation Monte Carlo (DSMC) code MONACO, developed at the University of Michigan [36]. Although the simulation does not account for ionization, the results are still indicative of general behavior of neutrals through the channel. These simulations are fully 3D, as nonuniformity caused by the inlets prevents a simple 2D simulation from being useful. Simulations were carried out on the Great Lakes supercomputing cluster at the University of Michigan, utilizing 48 cores. The mesh is unstructured and comprised of 1.7M volume cells. The simulations utilize ~22M particles with a timestep of 0.5 μs and have a sample period of 200,000 steps. We employed an auto-scaling feature to ensure that at least 10 particles are present in each cell for statistical significance. We ran two simulations: one for xenon gas, flowed into the anode at 300 K at a rate of 164 sccm, and another for krypton gas, flowed into the anode at 300 K at a rate of 189 sccm. For both simulations, temperatures measured during experiment were used for the inlet, anode, and channel. The kinetic diameter used for xenon is 574 pm, while for krypton the kinetic diameter is 476 pm [37]. The inlet is at the 12 o'clock position in Fig. 11.

The resultant neutral densities from the MONACO simulation are shown in Fig 11. The results indicate that the neutral densities across the channel are virtually identical for xenon and krypton at the exit plane; while we might expect that the neutral density of krypton to be lower due to its higher mobility, the higher volumetric flow required of krypton to reach the same power as xenon makes up for the difference and results in an equivalent neutral density profile at the exit plane. The comparable neutral densities indicate that the lower ionization in krypton is solely due to a lower ionization cross-section.

2. Radial Ionization Profile

Previous measurements of electron temperatures on a US and MS thruster indicate higher electron temperatures along centerline for the MS configuration compared to the US configuration [14]. Within the range of electron temperatures seen in the channel of a Hall thruster, the effective ionization cross-section of krypton changes more dramatically than that of xenon [15]. We therefore might expect that the gap in mass utilization efficiency between xenon and krypton would be mitigated when changing from a US thruster to an MS thruster, due to the higher electron temperature and therefore larger increase in ionization cross-section for krypton. However, our measured results as shown in Table 2 indicate that the gap between xenon and krypton mass utilization efficiencies remained virtually the same. By comparing the radial profiles of electron temperatures and ionization cross-sections, we can develop a better understanding of how the distributions of these variables—not just the measurements along centerline—affect the resultant mass utilization efficiency.

As the ionization cross-section is a function of electron temperature, we first need to obtain a profile of the electron temperature across the channel for the H9. We retrieved ionization cross-sections for xenon and krypton through the LXCat database; the Biagi, Hayashi, Puech, SIGLO, and TRINITI databases were used for xenon, and the Biagi, Morgan, and SIGLO databases used for krypton [15]. The datasets were then plotted, averaged, and fit with a piecewise polynomial function, shown in Fig. 12.

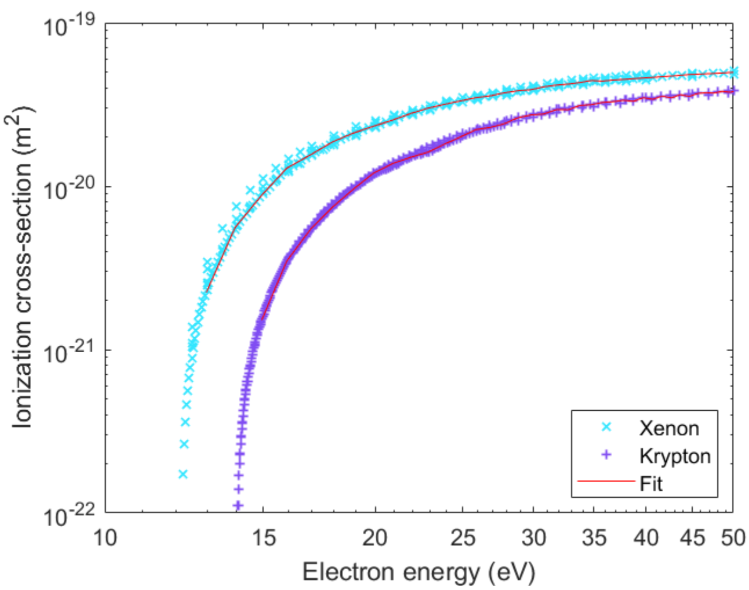

Fig. 12 Ionization cross-section as a function of electron temperature for xenon and krypton.

With this information, we can then input electron temperatures in the ionization region of the H9 to determine the radial profile of the ionization cross-section. These electron temperatures were retrieved from Hall2De, a 2-D axisymmetric fluid code that solves for the conservation equations of a partially ionized gas [13, 38, 39]. A simulation of the H9 was used as a reference for the magnetically-shielded case, while a simulation of the H6US—an unshielded thruster from which H9 derives a great deal of its design heritage [12, 13, 20, 31]—was used for the unshielded case. For both cases, the electron temperatures were extracted from a radial profile in the peak of the ionization region, taken to be the point of highest electron temperature along channel centerline. The electron temperature profiles are shown across a normalized radial profile in Fig. 13a. Because magnetic shielding causes cold electrons at the walls [13], the electron temperature approaches zero at the channel walls. The profiles also reflect previous experimental observations that the maximum centerline electron temperature is higher for a MS thruster than a US thruster [12]. These profiles allow us to estimate a comparison between the effective ionization across the channel for the unshielded case and the shielded case of xenon and krypton operation.

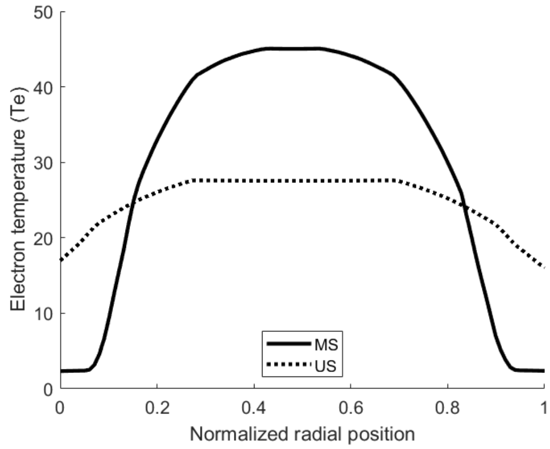

(a)

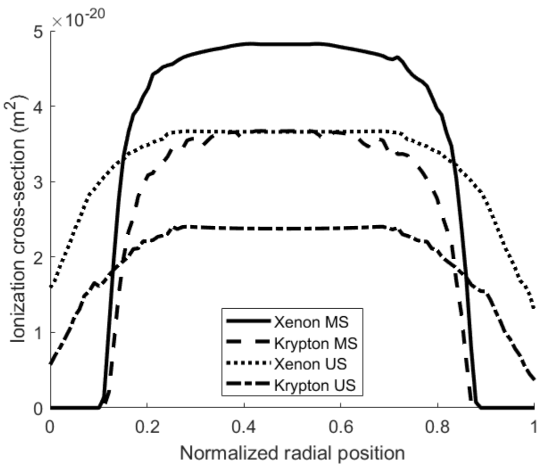

(b)

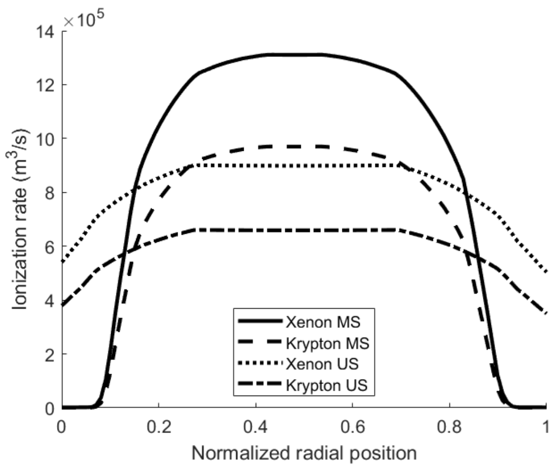

(c)

Fig. 13 Comparison of a) electron temperature, b) ionization cross-section, and c) ionization rate for xenon and krypton on an unshielded (US) and magnetically-shielded (MS) thruster as a function of normalized radial profile, where 0 is the inner channel radius and 1 is the outer channel radius.

By combining the results of Fig. 12 and Fig. 13a, we can plot profiles of the ionization cross-section across the channel for a shielded and unshielded thruster operating on both xenon and krypton. This result is shown in Fig. 13b. As expected from Eq. 10 and our results for neutral density, krypton's ionization cross-section on a MS thruster is lower than that of xenon at all points when comparing the US and the MS cases. Additionally, because of the low electron temperatures at the walls of the channel for the MS case, it is likely that very little ionization is occurring at the walls. However, our goal is to identify whether or not the *increase* in the *difference* between mass utilization efficiencies on krypton and xenon by changing from a US to MS thruster can be attributed to the profile of the ionization cross-section. Figure 13b indicates qualitatively that this may be a possibility, and previous studies [34] indicate that higher electron temperatures at the wall were necessary to improve the efficiency of krypton operation, which cannot be done with a shielded configuration. However, we still must quantify this difference on a US thruster versus on a MS thruster.

To this end, we can express the ion beam mass flow rate $\dot{m}_b$ as a function of the ionization rate k_{iz} (shown as a function of radius in Fig. 13c), which is in turn dependent on the ionization cross-section and electron temperature. To determine the ionization rate, we can assume a Maxwell-Boltzmann distribution function for the temperature over all energies as shown in Eq. 11:

$$f(T_e, \varepsilon) = 2\sqrt{\frac{\varepsilon}{\pi}}(k_B T_e)^{-3/2} \exp\Big(-\frac{\varepsilon}{k_B T_e}\Big) d\varepsilon. \tag{11}$$

The ionization rate itself is then a function of this distribution and the cross-section integrated over all energies:

$$k_{iz}(T_e, \varepsilon) = \int_0^\infty f(T_e, \varepsilon)\sqrt{\frac{2\varepsilon}{m_e}}\sigma_{iz}(\varepsilon) d\varepsilon, \tag{12}$$

and the beam ion mass flow rate can then be expressed as the following:

$$\dot{m}_b = 2\pi w_{iz} m_n \int_{r_i}^{r_o} n_n(r) n_e(r) k_{iz}(T_e(r), \varepsilon) r dr, \tag{13}$$

where w_{iz} is the width of the ionization region, m_n is the mass of the neutral, r_i and r_o are the inner and outer radii of the thruster respectively, n_n is the neutral density, and n_e is the electron density. Equation 13 can be combined with Eq. 6 to determine the mass utilization efficiency.

We compute a first-order approximation of the ratio between mass utilization efficiencies by assuming that the ionization region width, neutral density, and electron density are constant between xenon and krypton. This results in the following expression for the ratio of xenon over krypton mass utilization efficiency:

$$\frac{\Big(\eta_m\Big)_{Xe}}{\Big(\eta_m\Big)_{Kr}} = \frac{\Big(m_n\Big)_{Xe}\Big(\dot{m}_a\Big)_{Kr}\Big(\int_{r_i}^{r_o} k_{iz}(T_e(r)) r dr\Big)_{Xe}}{\Big(m_n\Big)_{Kr}\Big(\dot{m}_a\Big)_{Xe}\Big(\int_{r_i}^{r_o} k_{iz}(T_e(r)) r dr\Big)_{Kr}}. \tag{14}$$

We can then compare this ratio between the unshielded and shielded case from both the calculation using Eq. 14 and from the experimental results shown in Table 2. The mass flow rates used during operation were used as inputs into Eq. 14 for both the shielded and the unshielded case. The results are shown in Table 3.

Comparison	Method	Ratio
$\left[\frac{(\eta_m)_{Xe}}{(\eta_m)_{Kr}}\right]_{US}$	Calculated	1.57
$\left[\frac{(\eta_m)_{Xe}}{(\eta_m)_{Kr}}\right]_{MS}$	Calculated	1.56
$\left[\frac{(\eta_m)_{Xe}}{(\eta_m)_{Kr}}\right]_{US}$	Measured	1.13
$\left[\frac{(\eta_m)_{Xe}}{(\eta_m)_{Kr}}\right]_{MS}$	Measured	1.13

Table 3 Ratios of mass utilization efficiency between xenon and krypton for unshielded/magnetically-shielded configurations, where "Calculated" values are found using Eq. 14 and "Measured" values are found using values in Table 2.

The calculated values for the ratios are approximately 1.4× larger than the measured values, likely due to the assumptions we made regarding equivalent ionization widths, neutral densities, and electron densities between xenon and krypton. Previous results have in fact shown that krypton ionization regions tend to be wider than those of xenon [34, 35]. However, for a given method, we find that the ratios of η_m are approximately the same for the unshielded and shielded case. These results indicate that indeed, the lower electron temperatures at the walls that are required by magnetic shielding may be the cause of decreased effective ionization for krypton on a MS thruster compared to xenon, despite the higher temperatures along channel centerline. This provides at least preliminary evidence for the cause of the comparable gap in xenon and krypton mass utilization efficiencies on MS thrusters.

C. Strategies for Optimizing Krypton Performance

The results of our studies lend some guidance into how we may be able to improve the performance of krypton operation on shielded thrusters. The largest sources of efficiency loss for krypton compared to xenon are in its mass utilization efficiency and current utilization efficiency; therefore, any performance optimization effort for krypton should focus on trying to improve ionization in the channel and reduce electron current.

One method that has been previously used for improving the performance of unshielded Hall thrusters is lengthening the channels [10, 11]. Although this method proved to slightly decrease the divergence efficiency, it greatly improved the mass utilization efficiency and the overall anode efficiency for krypton operation by allowing more time for the krypton neutrals to ionize. One caveat to this method is that on a magnetically-shielded Hall thruster, the acceleration region may exist outside of the channel exit even with a longer channel, which may further worsen the divergence efficiency of krypton compared to xenon [12]. However, considering the gap in η_d between xenon and krypton is only 6% while the gap in η_m is 12%, it appears that maximizing η_m is the priority for krypton operation.

Another method of increasing the residence time could be through the application of an azimuthal swirl to the neutral injection. A previous study utilized a rotational propellant injector to increase the azimuthal velocity of neutrals in the channel [32]. This resulted in improved mass utilization efficiencies and divergence efficiencies, both of which would significantly benefit the operation of krypton on a shielded thruster. We may be able to leverage this technique and apply it to shielded Hall thrusters in a way that increases the residence time of krypton neutrals in the channel.

We could also focus the neutrals closer to centerline and not allow them to diffuse towards the edges of the channel as much through the use of a neutral injector in the center of the channel. The design of the H9 utilizes a baffle system behind the anode that ensures azimuthal uniformity in the neutral flow through the channel [20]. However, in light of the potential impact of low electron temperatures near the walls on the ionization of krypton, we may need to redesign an anode injector that maximizes neutral densities along centerline through the channel.

As for reducing the electron current, we are again limited by our current lack of understanding regarding electron mobility in Hall thrusters. Still, we may be able to leverage Hall2De simulations to determine if and why the electron mobility is higher for krypton MS operation and take steps to mitigate this in the future.

VII. Conclusions

We measured the anode and specific efficiencies of krypton and xenon performance on a magnetically-shielded 9-kW class Hall thruster in the Large Vacuum Test Chamber at the University of Michigan. The results showed that krypton's anode efficiencies were consistently 9-19% less than those of xenon, dropping off at the highest-power condition of 600 V, 15 A. Compared to the 5-15% gap in xenon and krypton anode efficiencies seen on unshielded Hall thrusters in previous studies, these differences are significantly larger.

In order to better characterize this efficiency gap, we measured the efficiency contributions at 300 V, 15 A for both xenon and krypton. The major gap in xenon and krypton efficiencies came from the differences in mass and current utilization efficiencies, which we postulate are due to the lower electron temperatures at the walls and higher electron mobility, respectively, for krypton operation on a shielded thruster. A smaller gap in divergence efficiency may be due to an acceleration region located further downstream on the MS krypton thruster. We carried out a neutral simulation to help rule out the possibility of lower neutral densities as the culprit of the difference in mass utilization efficiencies.

To our knowledge, this is the first published work measuring efficiencies of a magnetically-shielded Hall thruster operating on krypton. Our results and discussion point to some of the possible differences in the physics of xenon and krypton operation on a MS HET, allowing us to better understand and mitigate these issues for krypton. As the use of krypton on magnetically-shielded Hall thrusters would improve the accessibility of these devices by significantly lowering the cost of testing and operation, we propose some possible techniques of improving krypton performance on these thrusters based upon the findings from our study.

VIII. Acknowledgements

This work was supported by the Graduate Research Fellowship Program from the National Science Foundation and the National Defense Science and Engineering Graduate Fellowship through the Air Force Office of Scientific Research. The authors would like to thank Matthew Byrne and Dr. Ethan Dale for their invaluable contributions in troubleshooting, data collection, and data reduction. An additional thanks to all the members of Plasmadynamics and Electric Propulsion Laboratory for their discussions and support.

References

[1] Hargus, W. A., Azarnia, G. M., and Nakles, M. R., "Demonstration of Laser-Induced Fluorescence on a Krypton Hall Effect Thruster," *32nd International Electric Propulsion Conference*, Wiesbaden, Germany, 2011.

[2] Hofer, R. R., Peterson, P. Y., Jacobson, D. T., and Manzella, D. M., "Factors Affecting the Efficiency of Krypton Hall Thrusters," *46th Meeting of the APS Division of Plasma Physics*, Savannah, GA, 2004.

[3] Linnell, J. A., and Gallimore, A. D., "Efficiency Analysis of a Hall Thruster Operating with Krypton and Xenon," *Journal of Propulsion and Power*, Vol. 22, No. 6, 2006, pp. 1402–1418.

[4] Kamhawi, H., Haag, T., Jacobson, D., and Manzella, D., "Performance Evaluation of the NASA-300M 20 kW Hall Thruster," *47th AIAA/ASME/SAE/ASEE Joint Propulsion Conference & Exhibit*, American Institute of Aeronautics and Astronautics (AIAA), San Diego, CA, 2011.

[5] Nakles, M., Hargus, W., Delgado, J., and Corey, R., "A Performance and Plume Comparison of Xenon and Krypton Propellant on the SPT-100," *32nd International Electric Propulsion Conference*, American Institute of Aeronautics and Astronautics (AIAA), Wiesbaden, Germany, 2011.

[6] Saevets, P. A., Kim, V. P., Grdlichko, D. P., and Smirnov, P. G., "Investigation of a Low-power Thruster on Krypton Propellant," *6th Russian-German Conference on Electric Propulsion and Their Application*, Vol. 185, Elsevier Ltd, 2017, pp. 85–90.

[7] Andreussi, T., Giannetti, V., Leporini, A., Ducci, C., and Estublier, D., "Temporal Evolution of the Performance and Channel Erosion of a 5kW-Class Hall Effect Thruster Operating with Alternative Propellants," Rome, Italy, 2016.

[8] Bugrova, A. I., Bishaev, A. M., Desyatskov, A. V., Kozintseva, M. V., Lipatov, A. S., and Dudeck, M., "Experimental investigations of a krypton stationary plasma thruster," *International Journal of Aerospace Engineering*, 2013. https://doi.org/10.1155/2013/686132.

[9] Kurzyna, J., Jakubczak, M., Szelecka, A., and Dannenmayer, K., "Performance tests of IPPLM's krypton Hall thruster," *Laser and Particle Beams*, Vol. 36, No. 1, 2018, pp. 105–114. https://doi.org/10.1017/S0263034618000046.

[10] Jacobson, D. T., and Manzella, D. H., "50 kW Class Krypton Hall Thruster Performance," *39th AIAA/ASME/SAE/ASEE Joint Propulsion Conference and Exhibit*, NASA, Huntsville, Alabama, 2003.

[11] Peterson, P., Jacobson, D., Manzella, D., and John, J., "The Performance and Wear Characterization of a High-Power High-Isp NASA Hall Thruster," *41st AIAA/ASME/SAE/ASEE Joint Propulsion Conference & Exhibit*, American Institute of Aeronautics and Astronautics (AIAA), Tucson, AZ, 2005, pp. 2005–4243.

[12] Hofer, R. R., Goebel, D. M., Mikellides, I. G., and Katz, I., "Magnetic shielding of a laboratory Hall thruster. II. Experiments," *Journal of Applied Physics*, Vol. 115, No. 4, 2014.

[13] Mikellides, I. G., Katz, I., Hofer, R. R., and Goebel, D. M., "Magnetic shielding of a laboratory Hall thruster. I. Theory and validation," *Journal of Applied Physics*, Vol. 115, No. 4, 2014.

[14] Hofer, R., Goebel, D., Mikellides, I., and Katz, I., "Design of a Laboratory Hall Thruster with Magnetically Shielded Channel Walls, Phase II: Experiments," *48th AIAA/ASME/SAE/ASEE Joint Propulsion Conference & Exhibit*, American Institute of Aeronautics and Astronautics, Atlanta, GA, 2012.

[15] Bordage, M. C., Biagi, S. F., Alves, L. L., Bartschat, K., Chowdhury, S., Pitchford, L. C., Hagelaar, G. J., Morgan, W. L., Puech, V., and Zatsarinny, O., "Comparisons of sets of electron-neutral scattering cross sections and swarm parameters in noble gases: III. Krypton and xenon," *Journal of Physics D: Applied Physics*, Vol. 46, No. 33, 2013.

[16] Hofer, R. R., and Gallimore, A. D., "Efficiency Analysis of a High-Specific Impulse Hall Thruster," *40th Joint Propulsion Conference, AIAA-2004-3602*, American Institute of Aeronautics and Astronautics, Ft. Lauderdale, FL, 2004.

[17] Hofer, R. R., Katz, I., Mikellides, I. G., Goebel, D. M., Jameson, K. K., Sullivan, R. M., , and Johnson, L. K., "Efficacy of Electron Mobility Models in Hybrid-PIC Hall Thruster Simulations," *44th Joint Propulsion Conference, AIAA-2008-4924*, American Institute of Aeronautics and Astronautics, Hartford, CT, 2008.

[18] Hofer, R. R., "Development and Characterization of High-Efficiency, High-Specific Impulse Xenon Hall Thrusters," Ph.D. thesis, University of Michigan, 2004.

[19] Goebel, D. M., and Katz, I., *Fundamentals of Electric Propulsion: Ion and Hall Thrusters*, Jet Propulsion Laboratory, California Institute of Technology, Pasadena, CA, 2008.

[20] Hofer, R. R., Cusson, S. E., Lobbia, R. B., and Gallimore, A. D., "The H9 Magnetically Shielded Hall Thruster," *35th International Electric Propulsion Conference*, Atlanta, GA, 2017.

[21] Hofer, R. R., Goebel, D. M., and Walker, R. M., "Compact Lab6 Hollow Cathode for a 6-kW Hall Thruster," *54th JANNAF Propulsion Meeting*, 2018, pp. 14–17.

[22] Viges, E. A., Jorns, B. A., Gallimore, A. D., and Sheehan, J. P., "University of Michigan's Upgraded Large Vacuum Test Facility," *36th International Electric Propulsion Conference*, Vienna, Austria, 2019.

[23] Dankanich, J. W., Walker, M., Swiatek, M. W., and Yim, J. T., "Recommended practice for pressure measurement and calculation of effective pumping speed in electric propulsion testing," *Journal of Propulsion and Power*, Vol. 33, No. 3, 2017, pp. 668–680. https://doi.org/10.2514/1.B35478.

[24] Cusson, S. E., Hofer, R. R., Goebel, D. M., Georgin, M. P., Vazsonyi, A. R., Jorns, B. A., Gallimore, A. D., and Boyd, I. D., "Development of a 30-kW Class Magnetically Shielded Nested Hall Thruster," *36th International Electric Propulsion Conference*, Vienna, Austria, 2019.

[25] Xu, K. G., and Walker, M. L., "High-power, null-type, inverted pendulum thrust stand," *Review of Scientific Instruments*,

Vol. 80, No. 5, 2009. https://doi.org/10.1063/1.3125626.

[26] Lobbia, R. B., and Beal, B. E., "Recommended Practice for Use of Langmuir Probes in Electric Propulsion Testing," *Journal of Propulsion and Power*, Vol. 33, No. 3, 2017, pp. 566–581. https://doi.org/10.2514/1.B35531.

[27] Efron, B., and Tibshirani, R. J., *An Introduction to the Bootstrap*, 1993.

[28] Huang, W., Shastry, R., Soulas, G. C., and Kamhawi, H., "Farfield Plume Measurement and Analysis on the NASA-300M and NASA-300MS," *33rd International Electric Propulsion Conference*, Washington D.C., USA, 2013.

[29] Hofer, R. R., and Gallimore, A. D., "Recent Results from Internal and Very-Near-Field Plasma Diagnostics of a High Specific Impulse Hall Thruster," *28th International Electric Propulsion Conference*, Toulouse, France, 2003.

[30] Brown, D. L., and Gallimore, A. D., "Evaluation of Facility Effects on Ion Migration in a Hall Thruster Plume," *Journal of Propulsion and Power*, Vol. 27, No. 3, 2011, pp. 573–585.

[31] Cusson, S. E., Hofer, R. R., Lobbia, R., Jorns, B. A., and Gallimore, A. D., "Performance of the H9 Magnetically Shielded Hall Thrusters," *35th International Electric Propulsion Conference*, Atlanta, Georgia, 2017.

[32] Xia, G., Li, H., Ding, Y., Wei, L., Chen, S., and Yu, D., "Performance optimization of a krypton Hall thruster with a rotating propellant supply," *Acta Astronautica*, Vol. 171, 2020, pp. 290–299. https://doi.org/10.1016/j.actaastro.2020.03.021.

[33] Xia, G. J., Ning, Z. X., Zhu, X. M., Wei, L. Q., Chen, S. W., and Yu, D. R., "Effect of low-frequency oscillation on plasma focusing in krypton hall thruster," *Journal of Propulsion and Power*, Vol. 36, No. 1, 2020, pp. 25–32. https://doi.org/10.2514/1.B37599.

[34] Linnell, J. A., and Gallimore, A. D., "Internal plasma potential measurements of a Hall thruster using xenon and krypton propellent," *Physics of Plasmas*, Vol. 13, No. 9, 2006.

[35] Liu, D., Huffman, R. E., Branam, R. D., and Hargus, W. A., "Ultrahigh-speed imaging of hall-thruster discharge oscillations with krypton propellant," *IEEE Transactions on Plasma Science*, Vol. 39, No. 11 PART 1, 2011, pp. 2926–2927. https://doi.org/10.1109/TPS.2011.2146282.

[36] Dietrich, S., and Boyd, I., "Numerical simulations of Hall-effect plasma accelerators on a magnetic-field-aligned mesh," *Journal of Computational Physics*, Vol. 126, No. 2, 1996, pp. 328–342.

[37] Bird, G., *The DSMC Method*, 1.1, CreateSpace Independent Publishing Platform., 2013.

[38] Mikellides, I. G., and Katz, I., "Numerical simulations of Hall-effect plasma accelerators on a magnetic-field-aligned mesh," *Physical Review E - Statistical, Nonlinear, and Soft Matter Physics*, Vol. 86, No. 4, 2012.

[39] Ortega, A. L., and Mikellides, I. G., "A new cell-centered implicit numerical scheme for ions in the 2-D axisymmetric code Hall2De," *50th AIAA/ASME/SAE/ASEE Joint Propulsion Conference 2014*, American Institute of Aeronautics and Astronautics Inc., Cleveland, OH, 2014.